

# Optimization of Drag Reducing Shark Inspired Blade-Shape Riblet Surfaces in External Flow

M. Monfared<sup>1†</sup> and M. A. Alidoostan<sup>2</sup>

<sup>1</sup> Mechanical Engineering, Malek-Ashtar University of Technology, Shiraz, 7194915685, Iran

<sup>2</sup> Chemical Engineering, Malek-Ashtar University of Technology, Shiraz, 7194915685, Iran

†Corresponding Author Email: [mmonfared@mut.ac.ir](mailto:mmonfared@mut.ac.ir)

(Received March 10, 2019; accepted May 25, 2019)

## ABSTRACT

The main goal of this research is to study the drag reduction capabilities of blade-shape riblet surfaces in external flows. For this purpose, the ability of riblet surfaces for drag reduction of an underwater hydrodynamic model has been investigated. The surface geometry has been modified by applying shark skin inspired blade-shape riblets on the surface. These riblets have been modeled in various dimensions and applied on the exterior surface of an underwater hydrodynamic model, and their effects on the exerted drag force, at different flow velocities, have been studied numerically. For validating the numerical solution, the simulation results have been compared with the experimental data obtained by testing an underwater hydrodynamic model in a towing tank laboratory; and the validity of the numerical solution results has been confirmed. The results indicated that, riblet spacing has a significant effect on the reduction of drag force. Furthermore, by increasing the riblet spacing, the drag force is increased rather than decreased. Also, as the velocity increases, the performance of riblets in reducing the drag force is enhanced. In order to minimize the drag force applied on the underwater hydrodynamic model, by analyzing the numerical results, the most optimum riblet spacing has been obtained; at which the drag force is reduced by 7%. The achieved distance is a limit value; and at distances smaller or larger than this optimal distance, the effectiveness of the blade-shape riblet surface in reducing the drag force diminishes.

**Keywords:** Underwater hydrodynamic model; Towing tank laboratory; Drag reduction; Riblet surface; Numerical simulation.

## NOMENCLATURE

$C$	model coefficient	$Re_{\theta t}$	momentum thickness Reynolds number
$h$	height	$\gamma$	intermittency variable
$t$	time		
$u$	velocity	$\rho$	density
$S$	strain rate	$\mu$	viscosity
$E_{\gamma}$	destruction term	$\mu_t$	turbulent viscosity
$P_{\gamma}$	destruction term		

## 1. INTRODUCTION

Reducing the drag force applied on a body moving through a fluid and, consequently, achieving higher speeds and lower fuel consumption, has always been of interest to researchers. Moreover, by reducing the resistance or drag force, in addition to the abovementioned benefits, it is possible to travel longer distances, reduce the amount of environmental pollution, and to increase the lifespan and improve the performance of machines

and mechanical equipment.

Although novel methods and techniques for reducing the drag force on moving bodies presently exist, there is still ongoing research to reduce it even further and to improve the performance of manmade machines; and to this end, more effective techniques are being pursued and presented.

Different drag reduction techniques, such as complaints, hydrophobic paints, air lubricating, polymer solutions, soapy solutions, riblets, etc.,

have their own particular advantages and disadvantages.

Nature is full of wonderful and efficient patterns and structures that can be imitated to design and manufacture various industrial and commercial equipment. Plants, animals and natural phenomena have inspired multitudes of design engineers in recent decades. Optimal and efficient shapes as well as multiple functions constitute the prominent features of natural structures. The high speed and maneuverability of fishes, dolphins and sharks in water point out the drag reduction mechanisms that nature has endowed these animals. The microstructures that cover the skins of fast swimming sharks, and are known as dermal riblets, resemble small protrusions aligned with fluid flow.

Riblet surfaces contain regular microgrooves that form in streamwise direction on the surface. This type of cover has been imitated and adopted from shark skin. Fast swimming shark skin prevents the buildup of mosses and reduces the resistance and drag force caused by the movement of such quick animals through the water. By lifting and spinning the vortices, the small riblets covering a surface, reduce the amount of applied drag force, Bixler and Bushan-A (2013a).

Bechert *et al.* (2000) experimentally studied the drag reduction effects of trapezoidal-shape riblets surfaces. Only 64% of the test plate surface covered with riblets. The lateral spacing of the riblets on the test plate was  $s = 4.6$  mm. Experiments carried out in a wind tunnel and they found as much as 7.3% reduced turbulent shear stress, as compared to a smooth flat plate. The surfaces with tiny riblets aligned in the streamwise direction in an oil channel examined by Bechert *et al.* (1997). They reported that the blade shape riblet surface reduced drag by 9.9%. Suzuki and Kasagi (1994) investigated the turbulent flow field above the riblet surface by using the 3D PIV technique. It was concluded that at a certain lateral spacing of the riblets, the maximum turbulent intensities reduction near the riblet surface was achieved.

The flow structure of the wake behind a NACA 0012 airfoil covered with a V-shaped micro-riblet film considered experimentally by Lee and Jang (2005). The drag force was measured by using a three-component load-cell. The results revealed that riblets decreased the drag coefficient by 6.6% at  $Re = 1.54 \times 10^4$ . Han *et al.* (2003) conducted some experiments in closed-type subsonic wind tunnel to evaluate the drag reduction effects of micro riblets on the curved objects. Micro riblets was fabricated with polydimethylsiloxane (PDMS) micro molding technique on the  $6\text{cm} \times 6\text{cm}$  area. The height, spacing and length of the riblets were  $180\ \mu\text{m}$ ,  $300\ \mu\text{m}$ , and  $6\text{cm}$ , respectively. The drag reduction effects was examined using PIV technique and three-component load cell. The results indicated that riblets provided about 4.3% drag reduction on the airfoil and 7.6% drag reduction on the cylinder when the free stream velocities of the wind tunnel were 3.3 and 3m/s, respectively.

Walsh and Lindeman (1984) experimentally tested the drag reduction effects of V-shape riblet surfaces in both low speed and low turbulence wind tunnels. The results showed that the maximum drag reduction of 8% achieved for V-shape riblet at a specified height and spacing of the riblets. Drag reduction abilities of various shapes of the riblets such as sawtooth, scalloped and blade shapes considered by Dean and Bhushan (2010). The maximum drag reduction for blade-shape riblet at  $h/s \sim 0.5$ , scalloped-shape riblets at  $h/s \sim 0.7$  and sawtooth-shape riblets at angle of  $60^\circ$  were obtained nearly 10%, 6% and 5% respectively.

Liu *et al.* (1989) experimentally considered drag reduction in pipes lined with riblets. The results demonstrated that the maximum drag reduction of 5-7% was achieved for fully developed turbulent flow of water through 25.4 and 50.8-mm-diameters pipes lined with triangular-shape riblets.

Viswanath (2002) studied aircraft viscous drag reduction using riblets. The results achieved from wind tunnels and flight tests. They reported that skin friction drag reduction was in the range of 5–8% for 2D airfoils at low incidence and mild adverse pressure gradients. Wind tunnel experiments for a wind turbine airfoil associated with different riblet geometries carried out by Arndt *et al.* (2012). The most efficient riblet for a completely covered airfoil was found to be the V-groove shape of  $100\ \mu\text{m}$  height. It caused a drag reduction of 6% in the operational range expected for a turbine airfoil.

Fu *et al.* (2017) numerically studied the drag reduction capabilities of shark skin inspired riblet surfaces. The five types of riblet geometries included V, L, U,  $\cap$ , and  $\cup$  types were simulated numerically. It was observed that for a same spacing and flow velocity, the L geometry surface had best drag reduction performance. While the  $\cap$  geometry surface enhanced drag. Direct numerical simulation of turbulent flow over a riblet surface carried out by Goldstein *et al.* (1995). They analyzed the mean and fluctuating velocity and Reynolds shear stress profiles to evaluate the drag reduction abilities of riblet surfaces. The results indicated that the maximum drag reduction was near to 4%. Riblet drag reduction in mild adverse pressure gradients investigated numerically by Boomsma and Sotiropoulos (2015). They deduced that there was only a slight improvement in drag reduction for riblets in the mild adverse pressure gradients.

The interaction between turbulent flow and riblets, and its impact on their drag reduction properties are analyzed by Mayoral and Jimenez (2011). It was concluded that in small riblet spacing, the drag reduction is proportional to the riblet dimension, while for large riblet spacing the proportionality breaks down, and the drag reduction ultimately becomes an increase. Bixler and Bhushan-B (2013b) experimentally investigated the fluid drag reduction by using shark-skin riblet imitated microstructured surfaces. They considered the effects of riblet geometry, continuous and

segmented configurations, fluid velocity, fluid viscosity, closed channel height dimensions, wettability, and scalability on the drag reduction ability of riblet surfaces.

Turbulent skin friction drag reduction with longitudinal microgrooves and riblets in channel flow is analyzed using lattice Boltzmann method by Rastegary and Akhavan (2018). Turbulent boundary layer characteristics for a flat plate model with riblet surface is examined in wind tunnel experiments by Takahashi *et al.* (2018). The results revealed that skin friction drag is reduced about 3.6% at free stream velocity of 42m/s. Drag reductions of up to 61% is achieved in turbulent channel flow at Re-3600. Drag reducing riblet texture with fouling control properties is investigated by Benschop *et al.* (2018). Hydrodynamic drag measurement in Taylor-Couette set up revealed that the modified riblet reduced drag by up to 6% compared to a smooth surface. Large eddy simulation of 3-D V-shaped riblets is carried out by Smith *et al.* (2019). The investigated the V-shape grooves with height and spacing between 20 to 100 microns for aircraft applications.

Since, underwater hydrodynamic vehicles and drag reduction techniques are two main engineering problems in marine and hydrodynamic sciences, an underwater hydrodynamic model associated with riblet surfaces is selected to study both numerically and experimentally. In general, most of researches in drag reduction field, are related to the internal flows like micro channel flow. On the other hand, the majority of research in external flows is related to the aerial applications. Therefore, the innovation of this research is the use of riblet surfaces in marine applications and for an underwater hydrodynamic model in turbulent flow regime. The considered underwater hydrodynamic model has a maximum velocity of 25 m/s and, thus, it is subjected to a large drag force. In the present study, with regards to the manufacturing considerations, shark skin inspired blade-shape riblets with various dimensions have been modeled on the exterior surface of an underwater hydrodynamic model, and by numerically simulation, the optimal dimensions of riblets that minimize the drag force applied on the body at specified speeds have been achieved. For turbulence modeling, the 'Transition SST' model has been used, which has two equations for predicting the transition process and two equations for modeling turbulent flow characteristics. The obtained results have been validated by comparing them with experimental data. The findings of this research will provide the needed information for the engineers to design and fabricate an optimal and efficient prototype.

## 2. MODEL GEOMETRY, BOUNDARY CONDITIONS AND GOVERNING EQUATIONS

The model used in this research is an underwater hydrodynamic model with a length of 2880 mm and a circular cross section with a maximum diameter

of 64.8 mm (see Fig. 1). Due to the geometrical symmetry, only a quarter of the model has been numerically simulated.

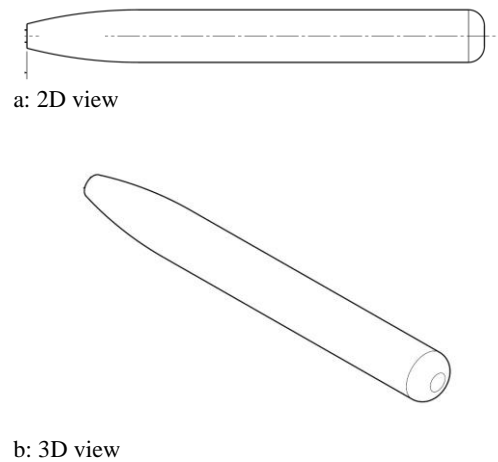


**Fig. 1. Geometry of the Investigated underwater hydrodynamic model.**

As is shown in Fig. 2, the blade-shape riblets on the surface of the model have a height of  $h$ , thickness of  $t$ , and spacing of  $s$ . The hydrodynamic model with the blade-shape riblet surface has been depicted in Fig. 3.

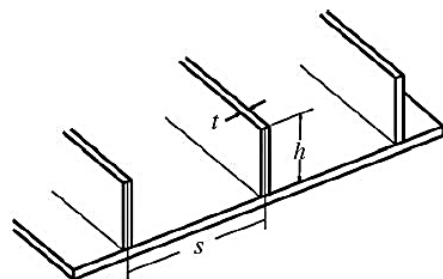


**Fig. 2. Schematic sketch of the studied blade-shape riblet, Bechert *et al.* (1997).**

In the computational domain, inlet velocity and outlet pressure boundary conditions have been applied at inlet and outlet, respectively. Also, the no-slip wall boundary condition, in which the normal and the tangential components of velocity are zero, has been set at the surface of the hydrodynamic model. The periodic boundary condition has been used for the lateral surfaces of the computational domain (see Fig. 4).

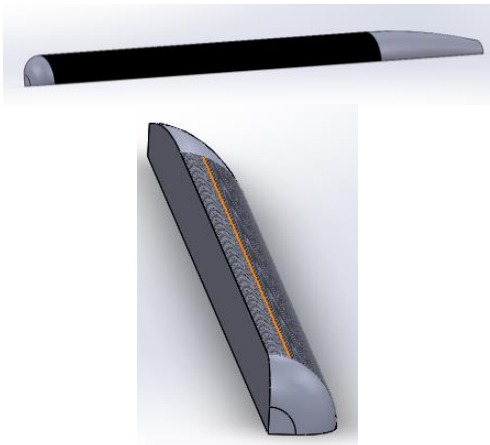
In the present study, the second order upwind scheme is applied for discretization and SIMPLE algorithm is employed to take account of pressure-velocity coupling. Also for turbulent incompressible flow, the transition SST model is used. The transition SST model is based on the coupling of SST  $k-\omega$  transport equations with two other transport equations, one for intermittency and one for the transition onset criteria, in terms of

momentum thickness Reynolds number. The transport equations for the intermittency  $\gamma$  and transition thickness Reynolds number  $Re_{\theta t}$  are defined by the following equations [Menter et al. \(2002\)](#):

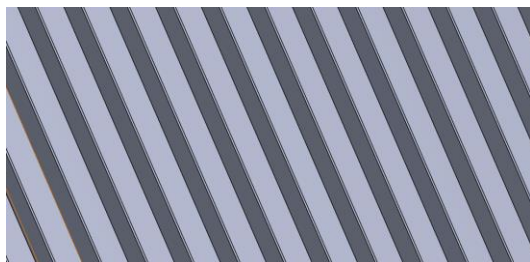
$$\frac{\partial(\rho\gamma)}{\partial t} + \frac{\partial(\rho u_i \gamma)}{\partial x_j} = C_{a1} F_1 \rho S (\gamma F_{set}) - C_{e1} P_{\gamma 1} \gamma + C_{a2} \rho \Omega \gamma F_t - C_{e2} P_{\gamma 2} \gamma + \frac{\partial}{\partial x_j} \left[ (\mu + \mu_t) \frac{\partial \gamma}{\partial x_j} \right] \quad (1)$$

$$\frac{\partial(\rho Re_{\theta t})}{\partial t} + \frac{\partial(\rho u_i Re_{\theta t})}{\partial x_j} = C_{\theta} \rho \left( \frac{\rho u_i^2}{500 \mu} \right) (Re_t - Re_{\theta t}) (1 - F_{\theta}) + \frac{\partial}{\partial x_j} \left[ \sigma_{Re} (\mu + \mu_t) \frac{\partial Re_{\theta t}}{\partial x_j} \right] \quad (2)$$

Where  $C_{a1}$ ,  $C_{e1}$ ,  $C_{e2}$ ,  $C_{\theta}$ ,  $F_t$ ,  $F_{\theta}$ ,  $P_{\gamma 1}$ ,  $P_{\gamma 2}$ ,  $\sigma_{\gamma}$  and  $\sigma_{Re}$  are the model coefficients [17].



a: Underwater hydrodynamic model



B Blade-shape riblet on the surface

**Fig. 3. Underwater hydrodynamic model with blade-shape riblet surfaces.**



**Fig. 4. Computational domain.**

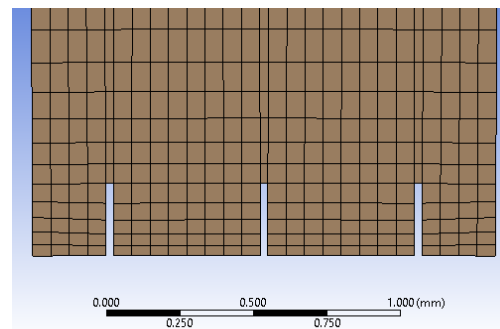
### 3. GRID GENERATION

Figure 5 shows the generated grid in a section of the computational domain around the body, and Fig. 6 illustrates the produced grid over the riblets. As expected, fine meshing should be used around the

hydrodynamic model and especially on the riblets; and this has been complied with, as shown in the following figures. Considering the geometry of the examined riblets, the total number of grid cells varies from 532962 to 2701660. To evaluate the mesh quality, its skewness measure, which is a number between 0 and 1, has been determined; the closer the skewness is to zero, the better the mesh quality. The average skewness for the present mesh is 0.008; which shows the very high quality of the produced mesh. The criterion of ‘Orthogonal Quality’, which is a number between 0 and 1, has also been investigated; the closer this measure is to one (1), the higher the quality of the applied mesh. The average orthogonal quality for the present mesh is 0.995.



**Fig. 5. Generated grid around the underwater hydrodynamic model.**



**Fig. 6. Generated grid near the riblets.**

### 4. VALIDATION

Experimental data which extracted from the experiments in towing tank laboratory have been used to validate the achieved numerical results. The experiments on the model have been performed in a rectangular towing tank with the dimensions of 150m × 7m. For moving the underwater hydrodynamic model in the water, a pylon has been attached to the end of the model (see Fig. 7). So the measured drag force is equal to the overall drag on the underwater hydrodynamic model and the pylon attached to it. The drag force on the driven model has been measured by a dynamometer, at a constant speed. The prepared numerical model has been depicted in Fig. 8. Due to the symmetry that exists in the problem, only half of the fluid domain has been simulated.

The experimental data and the numerical results related to the drag force applied on the underwater hydrodynamic model associated with pylon have been shown in Fig. 9 for different velocities. As it observed, there is a relatively good agreement between numerical results and experimental data; which indicates the validity of the numerical

solution method.



**Fig. 7. Underwater hydrodynamic model associated with pylon in the towing tank laboratory**

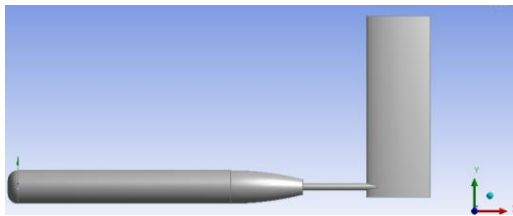


**Fig. 8. Underwater hydrodynamic model associated with pylon for numerical simulation.**

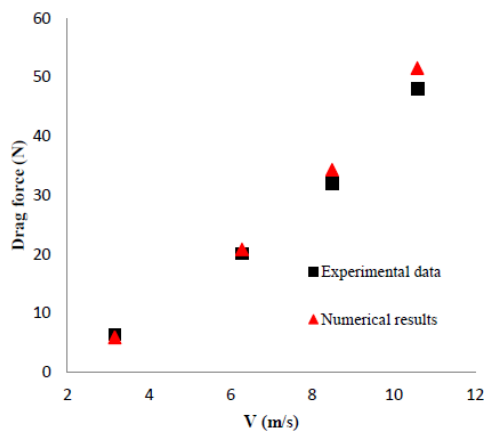


**Fig. 9. Comparison between experimental data and numerical results for drag force.**

### 5. GRID STUDY

In this section, the grid-independency of solution has been investigated for both a simple underwater hydrodynamic model (with a smooth surface) and a model with a riblet surface. The drag force results related to the simple underwater hydrodynamic model have been tabulated in Table 1 for various number of grid cells. It is observed that by making the grid size finer, the obtained results do not vary by much; therefore, the structured grid with

2701660 nodes is selected for the simple underwater hydrodynamic model.

The simulation details and the grid-independency of solution for the underwater hydrodynamic model with riblet surface have been illustrated in Table 2 and Fig. 11, respectively. For this case, a structured grid with 532962 nodes has been selected as the optimal grid; because the obtained results do not change significantly by making the mesh size any finer.

**Table 1 Drag coefficient results for simple model at different number of grid cells at V=10 m/s**

Number of Grid cells	$C_d$	Difference %
245035	0.168847	0
515475	0.15813	6.34715
1020225	0.150475	4.840941
2701660	0.145882	3.052326
5458120	0.145007	0.5997

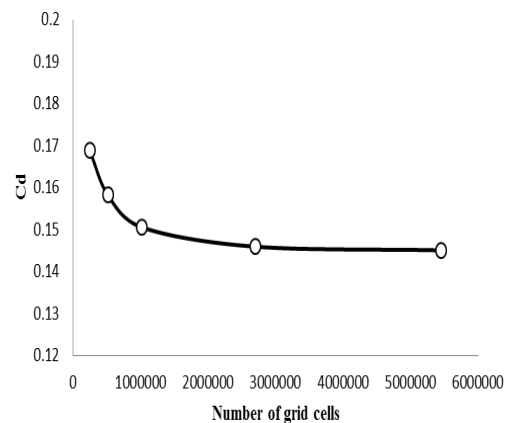


**Fig. 10. Drag coefficient results for simple model at different number of grid cells.**

**Table 2 Drag coefficient results for model with riblet surfaces at different number of grid cells at V=10 m/s**

Number of Grid cells	$C_d$	Difference %
245132	0.1211938	0
532962	0.1180581	2.587322
1171154	0.1175878	0.398406

### 6. RESULTS AND DISCUSSION

#### 6.1 Simple Underwater Hydrodynamic Model

The drag force coefficients obtained from the numerical solution for the simple underwater hydrodynamic model (with a smooth surface) have been listed in Table 3. The variations of

drag force coefficient with velocity (shown in Fig. 12) indicate that the drag coefficient decreases as the velocity increases. As an example, the velocity and pressure contours around the hydrodynamic body, from different views, have been plotted in Figs. 13, 14 and 15 for a velocity of 10 m/s.

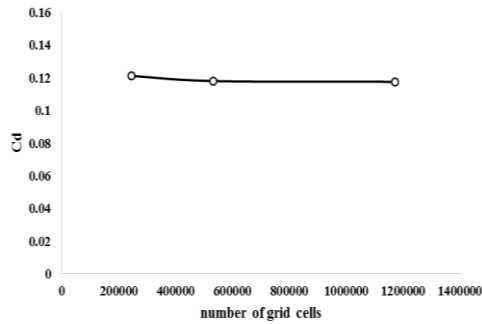


Fig. 11. Drag coefficient results for model with riblet surfaces at different number of grid cells.

Table 3 Drag force coefficient results for simple model at different velocities

Velocity m/s	$C_d$
5	0.13105
10	0.12167
15	0.11623
20	0.11292
25	0.11031

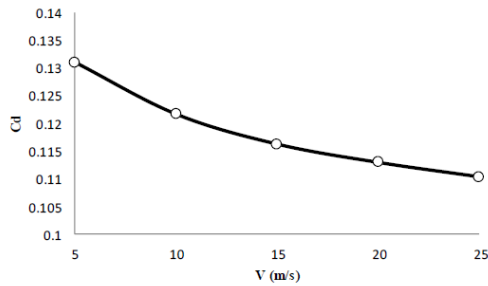


Fig. 12. Drag coefficient results for simple model at different velocities.

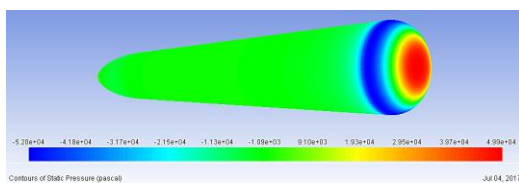


Fig. 13. Pressure distributions around simple model at velocity of 10 m/s.

## 6.2 Underwater Hydrodynamic Model with Riblet Surfaces

In this section, the numerical results for

underwater hydrodynamic model with blade-shape riblet surfaces have been analyzed and compared with each other. In all the performed simulations,  $h/s = 0.5$  and  $t/s = 0.05$ . Also the spacing of the riblets varied from  $100\mu\text{m}$  to  $2000\mu\text{m}$ .

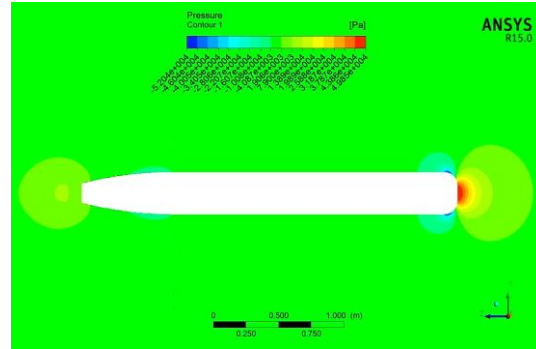


Fig. 14. 2-D pressure distributions around simple model at velocity of 10 m/s.

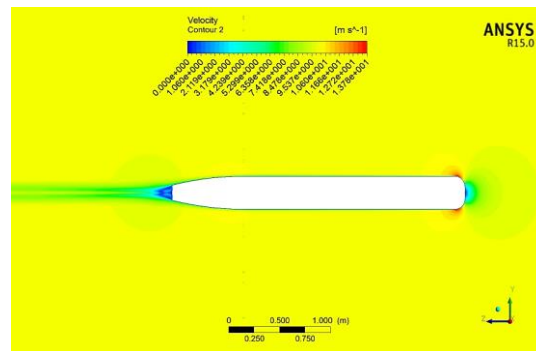


Fig. 15. 2-D velocity distributions around simple model at velocity of 10 m/s.

First, the effect of blade-shape riblet surface with  $s=2000\mu\text{m}$  on the underwater hydrodynamic model has been analyzed and the related results have been presented in Table 4. By comparing the obtained drag force coefficients with the data of the simple underwater hydrodynamic model, it is observed that, contrary to expectations, the presence of riblets at this distance leads to the increase of drag force and that enhancement is greater at lower velocities. The negative values in Table 4 indicate the increase of drag force. The main cause of this increase is the penetration of high-velocity fluid flow into the valleys and the increase of effective contact area in the high velocity regions.

Next, the influence of blade-shape riblet surfaces with  $s = 1000\mu\text{m}$  on the underwater hydrodynamic model has been studied and the associated results have been summarized in Table 5. The comparison among the drag coefficients obtained for the model with riblet

surface and the simple model shows a maximum drag force reduction of 3.95% at the velocity of 25 m/s.

**Table 4 Drag reduction capability of blade-shape riblet surfaces with  $s=2000\mu\text{m}$  at different velocities**

V (m/s)	Simple model	Model with riblet surfaces	Drag reduction (%)
5	0.1299916	0.1329613	- 1.46
10	0.1194354	0.122633	- 0.79
15	0.1141013	0.1162543	- 0.02
20	0.1096696	0.1135083	- 0.52
25	0.107067	0.1104673	- 0.14

**Table 5 Drag reduction capability of blade-shape riblet surfaces with  $s=1000\mu\text{m}$  at different velocities**

V (m/s)	Simple model	Model with riblet surfaces	Drag reduction (%)
5	0.1299916	0.1302197	0.63
10	0.1194354	0.1194278	1.84
15	0.1141013	0.1135502	2.31
20	0.1096696	0.1092932	3.21
25	0.107067	0.1059574	3.95

Then, the effect of surface blade-shape riblets with  $s=500\mu\text{m}$  has been examined and the relevant results have been illustrated in Table 6. Again, the comparison between the drag coefficients of the two models indicates a maximum drag force reduction of 4.67% in the model with riblet surface; which, similar to the preceding case, has occurred at the velocity of 25 m/s.

**Table 6 Drag reduction capability of blade-shape riblet surfaces with  $s=500\mu\text{m}$  at different velocities**

V (m/s)	Simple model	Model with riblet surfaces	Drag reduction (%)
5	0.1299916	0.1272132	2.92
10	0.1194354	0.1181651	2.88
15	0.1141013	0.1123727	3.32
20	0.1096696	0.1083305	4.06
25	0.107067	0.1051669	4.67

To further investigate the effect of riblets spacing on the drag reduction, the numerical analysis of flow has also been performed for three more cases ( $s = 300, 200$  and  $100 \mu\text{m}$ ) and the relevant results have been given in Tables 7, 8 and 9, respectively. As the findings indicate, the maximum reductions of drag

force for underwater hydrodynamic models that use riblets with spacing of  $s = 300 \mu\text{m}$ ,  $s = 200 \mu\text{m}$  and  $s = 100 \mu\text{m}$  are 4.99%, 6.78% and 5.42%, respectively.

**Table 7 Drag reduction capability of blade-shape riblet surfaces with  $s=300\mu\text{m}$  at different velocities**

V (m/s)	Simple model	Model with riblet surfaces	Drag reduction (%)
5	0.1299916	0.1265416	3.44
10	0.1194354	0.1174809	3.44
15	0.1141013	0.1116744	3.92
20	0.1096696	0.1077355	4.59
25	0.107067	0.10481	4.99

**Table 8 Drag reduction capability of blade-shape riblet surfaces with  $s=200\mu\text{m}$  at different velocities**

V (m/s)	Simple model	Model with riblet surfaces	Drag reduction (%)
5	0.1299916	0.1246009	4.92
10	0.1194354	0.1155827	5.00
15	0.1141013	0.1091703	6.08
20	0.1096696	0.1055838	6.50
25	0.107067	0.1028302	6.78

**Table 9 Drag reduction capability of blade-shape riblet surfaces with  $s=100\mu\text{m}$  at different velocities**

V (m/s)	Simple model	Model with riblet surfaces	Drag reduction (%)
5	0.1299916	0.1253464	4.35
10	0.1194354	0.1156651	4.94
15	0.1141013	0.110769	4.70
20	0.1096696	0.1077624	4.57
25	0.107067	0.1043331	5.42

Figure 16 demonstrates the comparison between drag reduction effects of riblet surfaces with various spacing. It is deduced that, applying riblet surfaces with large distances between ribs produces an opposite effect and leads to the increase of drag force. By reducing the distance between riblets, the riblet surfaces become more effective in reducing the amount of drag. However, this increased effectiveness has a limit value; and under limit conditions, the reduction of drag force diminishes by further reducing the distance between riblets. The optimal distance between riblets in studied model is  $s = 200 \mu\text{m}$ .

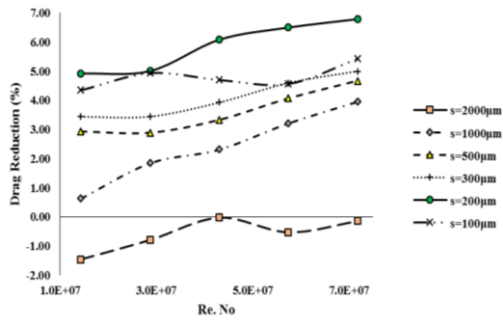
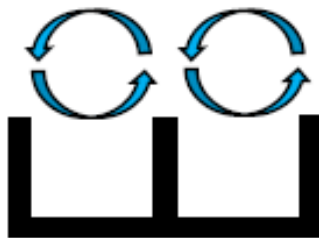


**Fig. 16. Comparison between drag reduction effects of riblet surfaces with various  $s$  in terms of Reynolds number.**

Drag reduction of riblet surfaces depend on the riblet spacing. When the vortices are lifted from the valley of riblets, causing reduction of friction drag by decreasing the ability of vortices to generate burst and sweep motions. For oversized riblets, the vortices are not away from the riblet surface, hence vortices are able to enter within the riblet spacing valley. As the vortex rotates in the valley, increased drag results due to the increase in burst and sweep motions. The differences in drag reduction are due to the riblet spacing, which are expected to decrease the effectiveness of lifting vortices. Figure 17 shows the schematic illustration of vortex lifting on the riblet surface.



a: smooth surface



b: riblet surface

**Fig. 17. Schematic illustration of drag reduction mechanism by riblet.**

To clarify the above description, in Fig. 18, the velocity distribution over the riblets for two important riblet spacing  $s=200\mu\text{m}$  and  $s=2000\mu\text{m}$  are illustrated. As it clear, for  $s=2000\mu\text{m}$ , the average diameter of the streamwise vortices above the wall are smaller than the spacing of the riblets, so the

streamwise vortices enter inside the riblet valleys. So the drag is enhanced. In contrast, for  $s=200\mu\text{m}$ , the average diameter of the streamwise vortices above the surface are larger than the spacing of the riblets, hence, majority of streamwise vortices will stay above the riblets, and only a limited area of the riblet tips is exposed to their induced sweep. Therefore, the drag is decreased.

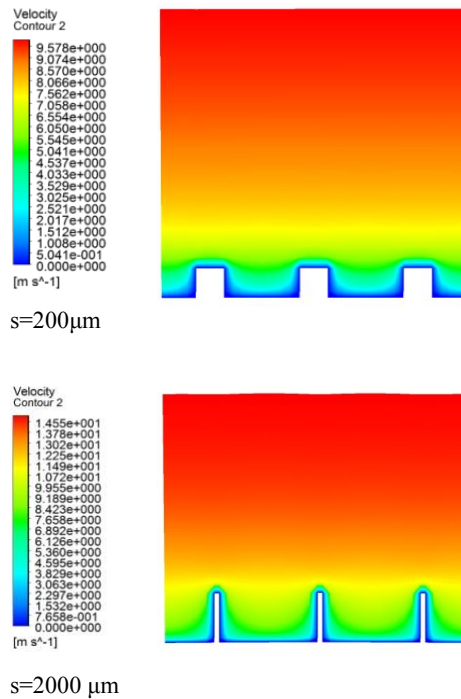


**Fig. 18. Velocity distribution over the riblet surfaces with different  $s$ .**

Figures 19 and 20 respectively show the contours of turbulent kinetic energy and eddy viscosity over the riblets at various  $s$ . By comparing the contours qualitatively and quantitatively, it is realized that by increasing the distance between two riblets, more turbulent flow enters the spaces between the valleys and adversely affects their performance.

## 7. CONCLUSION

In this study, blade riblets with different dimensions have been modeled on the exterior surface of an underwater hydrodynamic model, and by numerical simulations, the effects of these riblets on fluid drag force reduction at various velocities have been investigated. For validating the numerical approach, the obtained results have been compared with the experimental data obtained from the experiments which are carried out on

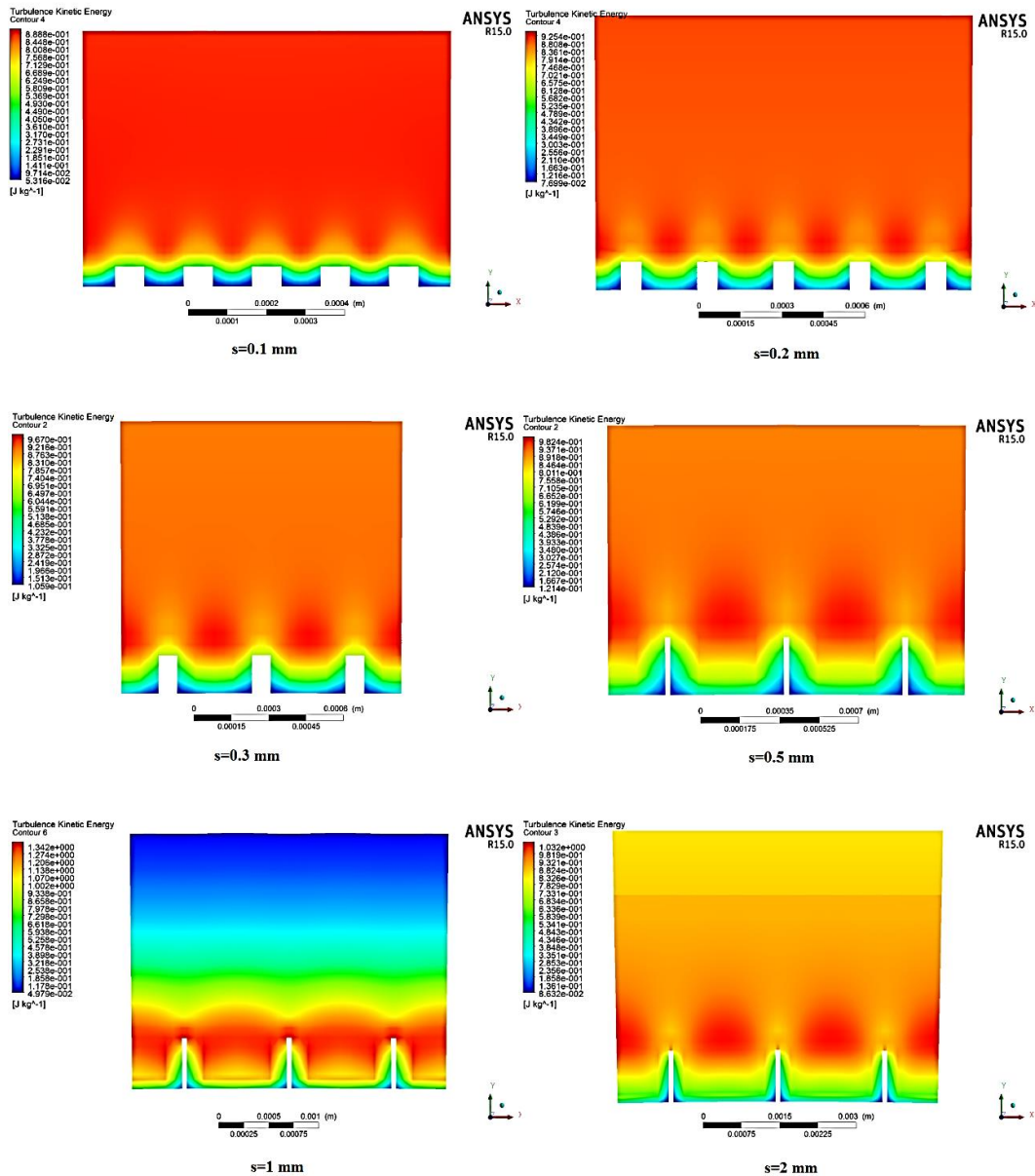


Fig. 19. Turbulent kinetic energy contours over the riblet surfaces with different  $s$  at velocity of 15m/s.

the underwater hydrodynamic model in the towing tank laboratory and the validity of the numerical results has been confirmed. Then, the drag force coefficients of model with riblet surfaces in various geometrical dimensions are calculated and compared with those of the simple underwater hydrodynamic model with a smooth exterior surface. The findings indicate that the distance between two riblets has a significant effect on the reduction of drag force. The results also show that riblet surfaces with large distances between their riblets have an adverse effect on drag reduction and actually increase the drag force applied on the hydrodynamic model. By reducing the distance between riblets, the drag force exerted on the model decreases; and at a limit point,

this drag reduction gets to be maximum. At the most effective distance between two riblets, which is about 200  $\mu\text{m}$ , the drag force applied on model is approximately reduced by 7%. By further reducing the distance between riblets below 200  $\mu\text{m}$ , the riblet surface becomes less effective in reducing the drag. Moreover, with the increase of velocity, the effectiveness of riblet surfaces in reducing the drag force is enhanced; which is due to the riblets interacting with flow vortices and preventing high-speed flows from entering the valleys between riblets. This causes the model surface to mostly contact the low-velocity regions of flow, and thereby reduces the drag force applied on the hydrodynamic model.

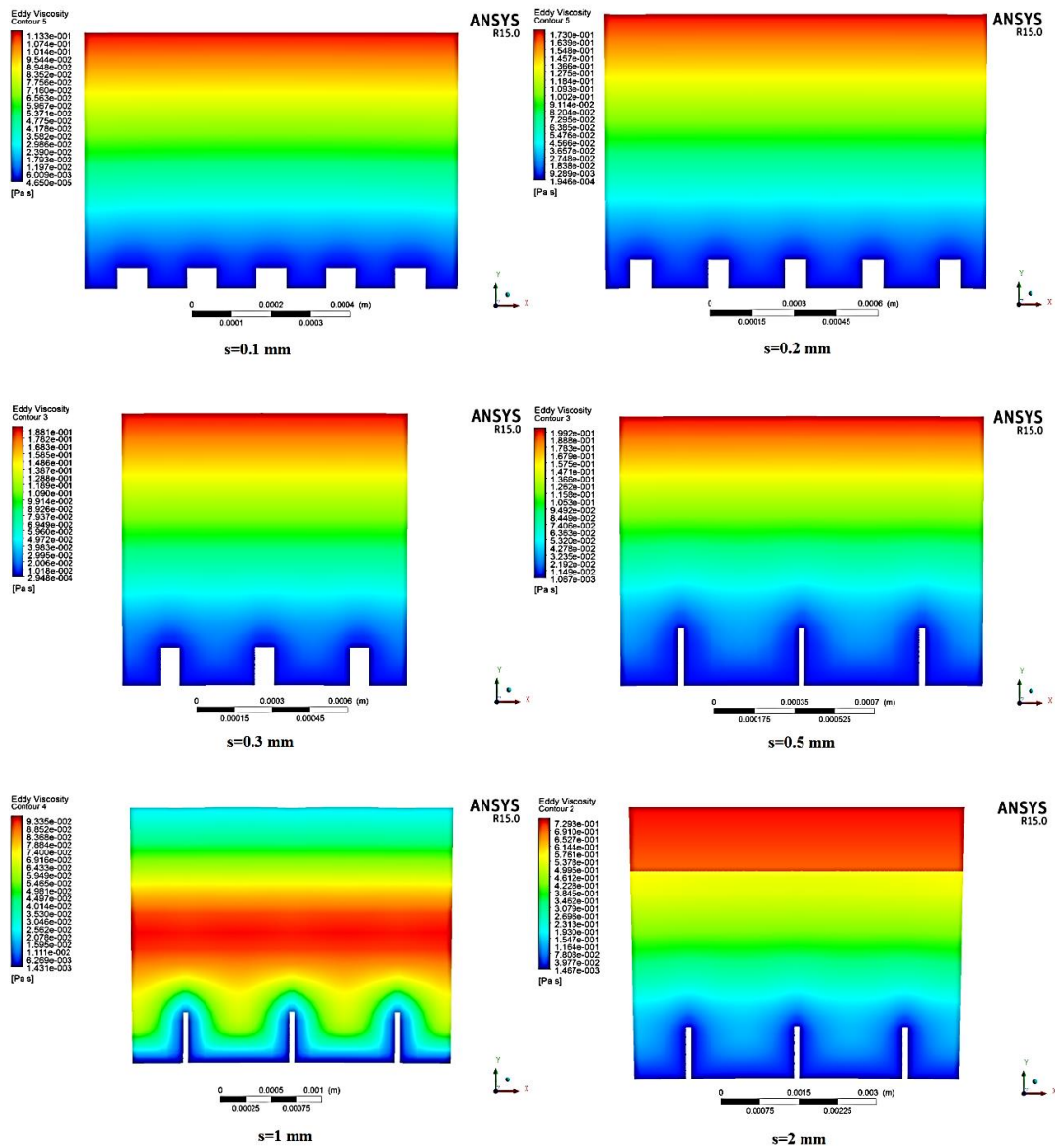


Fig. 20. Eddy viscosity contours over the riblet surfaces with different  $s$  at velocity of 15m/s.

## REFERENCES

- Arndt, P., L. P. Chamorro and F. Sotiropoulos (2012). Drag reduction in large wind turbines through riblets: evaluation of different geometries, *50th AIAA Aerospace Sciences Meeting including the New Horizons Forum and Aerospace Exposition*, Nashville, Tennessee, AIAA 2012-0232.
- Bechert, D. W., M. Bruse and Hage, W. (2000). Experiments with three-dimensional riblets as an idealized model of shark skin. *Experiments in Fluids* 28(5), 403–412.
- Bechert, D. W., M. Bruse, W. Hage, J. G. T. Van Der Hoeven and G. Hoppe, G. (1997). Experiments on drag reducing surfaces and their optimization with an adjustable geometry. *Journal of Fluid Mechanics* 338, 59–87.
- Benschop, H. O. G., A. J. Guerin, A. Brinkmann, M. L. Dale, A. A. Finne, W. P. Breugem, A. S. Clare, C. Price and K. J. Reynolds (2018). Drag reducing riblet texture with flouling-release: development and testing. *Biofouling* 34(5), 532–544.
- Bixler, G. D. and B. Bhushan (2013a). Fluid Drag Reduction with Shark-Skin Riblet Inspired Microstructured Surfaces. *Advanced Functional Material* 23(36), 4507-4528.
- Bixler, G. D. and B. Bhushan (2013b). Shark skin inspired low-drag microstructured surfaces in closed channel flow, *Journal of Colloid and Interface Science* 393, 384-396.
- Boomsma, A. and F. Fotis Sotiropoulos (2015),

- Riblet drag reduction in mild adverse pressure gradients: A numerical Investigation. *International Journal of Heat and Fluid Flow* 56, 251–260.
- Dean, B. and B. Bhushan (2010). Shark-skin surfaces for fluid-drag reduction in turbulent flow: a review. *Philosophical Transactions of the Royal Society A* 368(1929), 4775-4806.
- Fu, Y. F., C. Q. Yuan and X. Q. Bai, (2017). Marine drag reduction of shark skin inspired riblet surfaces. *Biosurface and Biotribology* 3(1), 11-24.
- Goldstein, D., R. Handler and L. Sirovich (1995). Direct numerical simulation of turbulent flow over a modeled riblet covered surface. *Journal of Fluid Mechanics* 302, 333-376.
- Han, M., F. C. Lim, Y. Jang, S. S. Lee and S. Lee (2003). Fabrication of a micro-riblet film and drag reduction effects on curved objects, *The 12<sup>th</sup> International Conference on Solid State Sensors, Actuators and Microsystems*, Boston.
- Lee, S. J. and Y. G. Jang (2005). Control of flow around a NACA 0012 airfoil with a micro-riblet film. *Journal of Fluids and Structures* 20(5), 659-672.
- Liu, K. N., C. Christodoulout, O. Ricciust and D. D. Joseph (1989). Drag Reduction in Pipes Lined with Riblets. *AIAA Journal* 28(10), 1697-1698.
- Mayoral, R. G. and J. Jimenez (2011). Drag reduction by riblets. *Philosophical Transactions of the Royal Society A* 369(1940), 1412-1427.
- Menter, F. R., T. Esch and S. Kubacki (2002). Transition Modeling Based on Local Variables. *5<sup>th</sup> International Symposium on Engineering Turbulence Modelling and Measurements*. Mallorca, Spain.
- Rastegary, A. and R. Akhavan (2018). The common mechanism of turbulent skin friction drag reduction with super hydrophobic longitudinal microgrooves and riblets. *Journal of Fluid Mechanics* 838, 68-104.
- Smith, B. R., P. J. Yagle and P. D. McClure (2019). Computational simulation of 3-D riblets for skin friction drag reduction. *AIAA* 1627-2019.
- Suzuki, Y. and N. Kasagit (1994). Turbulent drag reduction mechanism above a riblet Surface. *American Institute of Aeronautics and Astronautics Journal* 32(9), 1781-1790.
- Takahashi, H., M. Kurita, S. Koga and S. Endo (2018). Evaluation of skin friction drag reduction in turbulent boundary layer using riblets. *AIAA*.
- Viswanath, P. R. (2002). Aircraft viscous drag reduction using riblets, *Progress in Aerospace Sciences* 38, 571.
- Walsh, M. J. and A. M. Lindemann (1984). Optimization and application of riblets for turbulent drag reduction, *In AIAA 22<sup>nd</sup> Aerospace Sciences Meeting*, Reno, NV, 9–12 January, paper no. AIAA-84-0347.